

Early bounce of droplets on elastic plates: the role of momentum morphology and predictive modelling

Yufei Ma¹ and Haibo Huang¹

¹Department of Modern Mechanics, University of Science and Technology of China, Hefei, Anhui 230026, PR China

Corresponding author: Haibo Huang, huanghb@ustc.edu.cn

(Received 9 May 2025; revised 26 September 2025; accepted 2 October 2025)

This study investigates droplet impact on elastic plates using a two-phase lattice Boltzmann method in both two-dimensional (2-D) and three-dimensional (3-D) configurations, with a focus on rebound dynamics and contact time. The 2-D simulations reveal three distinct rebound modes – conventional bounce, early bounce and rim rising – driven by fluid–structure interaction. Among them, the early bounce mode uniquely achieves a significant reduction in contact time, occurring only at moderate plate oscillation frequency. Momentum analysis shows a non-monotonic relationship between vertical momentum transfer and rebound efficiency: increased momentum does not necessarily promote rebound if it concentrates in a central jet, which contributes minimally to lift-off. This introduces a novel rebound mechanism governed by momentum distribution morphology rather than total magnitude. A theoretical model treating the droplet–plate system as coupled oscillators is developed to predict contact time in the early bounce regime, showing good agreement with numerical results. The mechanism and model are further validated through fully 3-D simulations, confirming the robustness of the findings.

Key words: flow-structure interactions, drops

1. Introduction

The impact of liquid droplets on solid surfaces is a common phenomenon observed in both nature and industry. Examples include raindrops striking soil (Joung & Buie 2015), inkjet printing (Derby 2010; Sousa *et al.* 2014; Lohse 2022), spray coating (Dhiman, McDonald & Chandra 2007; Ye & Domnick 2017), pesticide application (Nuyttens *et al.* 2007; Massinon & Lebeau 2012) and bloodstain pattern analysis (Laan *et al.* 2014). This problem has attracted sustained interest in fluid dynamics for decades (Yarin 2006;

Josserand & Thoroddsen 2016; Cheng, Sun & Gordillo 2022; Lohse 2022). Upon impact, a droplet may deposit, rebound or splash (Josserand & Thoroddsen 2016), depending on various factors such as its viscosity (μ_H), surface tension (σ), density (ρ_H), initial size (the diameter D_0), impact velocity (U_0) and the characteristics of the surface. The dynamics of this process are primarily governed by inertial, viscous and capillary forces, which are often described using key dimensionless parameters. Among these, the Weber number ($We = \rho_H U_0^2 D_0 / \sigma$) characterizes the relative importance of inertial forces to surface tension, while the Reynolds number ($Re = \rho_H U_0 D_0 / \mu_H$) represents the ratio of inertial to viscous forces.

When droplets impact superhydrophobic or non-wetting surfaces at a relatively low velocity, they initially spread, reach a maximum diameter (Clanet *et al.* 2004) and then retract. In some cases, if the droplet is not too viscous or heavy, it fully bounces off due to the restoring force of surface tension (Richard & Quéré 2000; Biance *et al.* 2006; Sanjay, Chantelot & Lohse 2023). This rebound mechanism is commonly observed in nature, allowing plants and animals to repel water and stay dry (Quéré 2008; Bird *et al.* 2013; Wisdom *et al.* 2013). It also finds widespread industrial applications, such as anti-icing surfaces (Mishchenko *et al.* 2010; Kreder *et al.* 2016), self-cleaning technologies (Blossey 2003; Bhushan & Jung 2011), heat transfer enhancement (Zhang *et al.* 2016; Liang & Mudawar 2017) and directional droplet transport (Li *et al.* 2016; Sun *et al.* 2019).

A key factor in these applications is the droplet's contact time, t_c , which represents the duration between initial impact and departure from the surface. Richard, Clanet & Quéré (2002) were among the first to experimentally demonstrate that contact time is primarily influenced by droplet size rather than impact velocity. This behaviour can be modelled using an inertia—capillarity time scale,

$$t_c = a\sqrt{\frac{\rho_H D_0^3}{\sigma}},\tag{1.1}$$

where *a* is an experimentally determined prefactor, independent of impact velocity at the inertia–capillary regime (moderate and high Weber numbers) (Richard *et al.* 2002; Abolghasemibizaki *et al.* 2019). While at low Weber numbers (viscous–capillary regime) *a* acquires a velocity dependence (Abolghasemibizaki *et al.* 2019). Although contact times are typically of the order of milliseconds, significant energy, momentum and mass exchanges occur between the droplet and the surface (Voigt *et al.* 2011; Shiri & Bird 2017).

For many industrial applications, minimizing contact time is beneficial. For instance, ice accumulation on surfaces can pose serious challenges for aircraft (Mohseni & Amirfazli 2013), transmission lines (Wei *et al.* 2016) and wind turbines (Kraj & Bibeau 2010). Reducing ice formation requires rapid shedding of impacting droplets (Maitra *et al.* 2014*a*). Studies have shown that at the same surface temperatures, droplets on superhydrophobic surfaces can rebound before freezing, whereas ice nucleates on smooth hydrophilic and hydrophobic surfaces (Mishchenko *et al.* 2010).

Consequently, reducing droplet contact time (t_c) has become a central goal in many related applications. Based on the interaction mechanisms between the impacting droplet and the surface, research in this area can be broadly categorized into three main strategies (Fan *et al.* 2023): (i) surfaces patterned with micro/nanotextures (Li, Ma & Lan 2010; Liu *et al.* 2014; Moqaddam, Chikatamarla & Karlin 2017); (ii) axisymmetry breaking (Bird *et al.* 2013; Liu *et al.* 2015; Gauthier *et al.* 2015; Zhan *et al.* 2021); (iii) the use of elastic surfaces (Weisensee *et al.* 2016; Vasileiou *et al.* 2016; Xiong, Huang & Lu 2020).

The first strategy involves micro/nanotextured surfaces, where part of the droplet penetrates into the surface texture, storing capillary energy within the liquid. This stored

energy is then converted into kinetic energy, facilitating a more rapid upward motion and faster detachment. For instance, Liu *et al.* (2014) experimentally demonstrated that droplets impacting surfaces with submillimetre-scale textured posts decorated with nanostructures can bounce off in a pancake-like shape without significant retraction, reducing contact time by a factor of four compared with conventional rebounds. The latter typically involve symmetric spreading and full retraction on flat, superhydrophobic rigid surfaces. Similarly, Moqaddam *et al.* (2017) observed a nonlinear relationship between contact time and *We* in simulations at higher *We*. Additionally, hierarchical and densely packed nanoscale textures have been shown to significantly decrease contact time (Lv *et al.* 2016; Wang *et al.* 2020).

The second strategy, breaking axisymmetry, accelerates droplet recoil by disrupting the uniform inward retraction seen in axisymmetric impacts. In symmetric cases, the droplet's edge retracts uniformly at a constant velocity. However, when asymmetry is introduced, retraction occurs more rapidly along specific directions, leading to a faster rebound (Bird et al. 2013). Various methods have been employed to induce this asymmetry. For instance, Bird et al. (2013) introduced surface ridges on the scale of the spreading drop's film thickness. These ridges lead to localized variations in film thickness that accelerate retraction along specific paths along the ridge direction than in other areas, thereby breaking radial symmetry and enhancing recoil efficiency. Similarly, Liu et al. (2015) investigated droplet impacts on curved surfaces with a curvature comparable to the droplet size. They found that liquid retracts more quickly along the axial direction, reducing contact time compared with impacts on flat surfaces. Another approach involves dynamic surfaces. Zhan et al. (2021) demonstrated that a horizontally moving surface stretches the droplet's front lamella along the motion direction, keeping it farther from the droplet bulk. This early dewetting initiation leads to a faster rebound compared with stationary surfaces. Additionally, oblique impacts have been shown to effectively reduce contact time by naturally breaking axisymmetry (Regulagadda, Bakshi & Das 2018).

The third strategy for reducing droplet contact time involves using elastic surfaces. Unlike rigid surfaces, elastic surfaces deform upon impact, temporarily storing energy that is subsequently transferred back to the droplet through upward motion, enhancing its rebound. This early-lift mechanism, termed the 'springboard effect' by Weisensee *et al.* (2016), was also associated with the 'pancake bouncing' phenomenon. Similarly, Vasileiou *et al.* (2016) demonstrated that when the oscillation frequencies of the elastic surface and the droplet are synchronized, surface repellency is enhanced, providing additional energy for the droplet's rebound. Upadhyay, Kumar & Bhardwaj (2021) further explored this interaction by studying droplets bouncing on an elastic cantilever beam and developing a spring—mass model to describe the dynamic coupling between the droplet and the surface. Additional experimental studies have reinforced the effectiveness of elastic surfaces in reducing contact time (Kim, Rothstein & Shang 2018; Huang *et al.* 2018). Other studies also examine droplet impact on flexible substrates (see Gart *et al.* 2015, Dressaire *et al.* 2016), which also show the significant effect of substrate flexibility on droplet dynamics.

While the first two strategies have been extensively investigated through both experiments and simulations, numerical studies on droplet rebound from elastic surfaces remain limited. In particular, the early-lift mechanism, or 'springboard effect' (Weisensee et al. 2016), remains poorly understood. Compared with experiments, numerical simulations can provide more detailed quantitative insights into droplet dynamics, helping to elucidate the key mechanisms responsible for faster rebounds on elastic surfaces. To date, the only relevant numerical study was conducted by Xiong et al. (2020), which focused on two-dimensional (2-D) simulations. However, due to the low We used in the study, it failed to capture the experimentally observed pancake bounce – the phenomenon responsible for the greatest reduction in contact time. To bridge this gap,

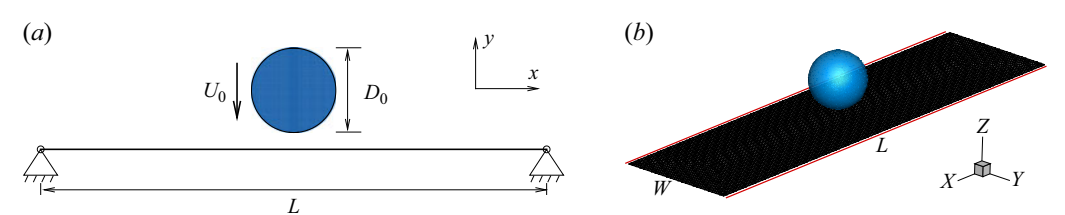


Figure 1. Schematic diagram of a droplet impacting an elastic plate. (a) The 2-D case. (b) The three-dimensional (3-D) case, where the two edges marked by red lines are free, while the other two edges are simply supported. Here, L and W represent the length and width of the plate, respectively.

further simulations covering a broader range of *We* are needed, along with a deeper understanding of the early-lift mechanism.

In this study, we simulate droplet impact on elastic plates at moderate We using the phase-field lattice Boltzmann method (LBM). Our focus is to investigate how surface motion influences the rebound process and contact time. By analysing the detailed flow field within the droplet, our simulations provide valuable insights into the underlying dynamics of early bouncing. Furthermore, we develop a theoretical model to predict the contact time for droplets impacting elastic surfaces. This work aims to offer a comprehensive understanding of droplet rebound dynamics, contributing to the optimization of industrial applications such as anti-icing surface design and self-cleaning technologies.

2. Methodology

A schematic diagram of a droplet impacting an elastic plate is shown in figure 1(a). The droplet, with an initial diameter D_0 , impacts the plate with a downward velocity U_0 . Initially, the droplet is positioned above the centre of the elastic plate. Gravity is neglected in this study because the droplet diameter is much smaller than the capillary length $l_c = \sqrt{\sigma/(\rho_H g)}$, and the Bond number follows $Bo^2 \ll We$ (Molacek & Bush 2012), where $Bo = \rho_H g D_0^2/\sigma$ and g is the gravitational acceleration. Under these conditions, surface tension dominates and gravitational effects are negligible. The plate has an initial length L, with both ends simply supported. Figure 1(b) illustrates the 3-D set-up, where the two ends are simply supported, while the other sides (marked by red lines) are free.

In our simulations, we employ the phase-field LBM (Liang *et al.* 2018) to solve the fluid flow and the finite element method (Doyle 2001) to model the deformation and motion of the elastic plate. To track the fluid interface, we use the conservative phase-field Allen–Cahn equation (Xiong *et al.* 2020; Ma & Huang 2023),

$$\frac{\partial \phi}{\partial t} + \nabla \cdot (\phi \mathbf{u}) = \nabla \cdot \left[M \left(\nabla \phi - \frac{4}{\xi} \phi (1 - \phi) \hat{\mathbf{n}} \right) \right], \tag{2.1}$$

where ϕ is the phase-field variable, varying from 0 (vapour) to 1 (liquid). The densities of the vapour and liquid phases are denoted as ρ_L and ρ_H , respectively. Here, \boldsymbol{u} represents the macroscopic velocity vector, \boldsymbol{M} is the mobility, $\boldsymbol{\xi}$ is the interface thickness and $\hat{\boldsymbol{n}}$ is the unit normal vector to the fluid interface, defined as $\nabla \phi/|\nabla \phi|$, pointing towards the liquid phase.

The isothermal, incompressible Navier–Stokes equations are also solved using the LBM framework (Xiong *et al.* 2020; Ma & Huang 2024). The motion and deformation of the elastic plate in both 2-D and 3-D cases are governed by the structural (2.2) and (2.3),

respectively (Hua, Zhu & Lu 2014; Xiong et al. 2020),

$$\rho_{s}h_{s}\frac{\partial^{2}X}{\partial t^{2}} - \frac{\partial}{\partial s}\left[Eh_{s}\left(1 - \left|\frac{\partial X}{\partial s}\right|^{-1}\right)\frac{\partial X}{\partial s}\right] + EI\frac{\partial^{4}X}{\partial^{4}s} = F_{ext}, \quad \text{2-D}, \quad (2.2)$$

$$\rho_{s}h_{s}\frac{\partial^{2}X}{\partial t^{2}} - \sum_{i,j=1}^{2}\left[\frac{\partial}{\partial s_{i}}\left(Eh_{s}\varphi_{ij}\left[\delta_{ij} - \left(\frac{\partial X}{\partial s_{i}} \cdot \frac{\partial X}{\partial s_{j}}\right)^{-1/2}\right]\frac{\partial X}{\partial s_{j}} - \frac{\partial}{\partial s_{j}}\left(EI\gamma_{ij}\frac{\partial^{2}X}{\partial s_{i}\partial s_{j}}\right)\right)\right]$$

$$= F_{ext}, \quad \text{3-D}, \quad (2.3)$$

where s is the Lagrangian coordinate along the plate direction, X is the position vector of the plate, ρ_s is the plate density, h_s is the plate thickness, EI and Eh_s are the bending and stretching stiffnesses, respectively, where $I=h_s^3/12$ and E is Young's modulus. Here φ_{ij} and γ_{ij} are the in-plane and out-of-plane effect matrices, respectively. And their components are $\varphi_{11}=\varphi_{22}=1$, $\varphi_{12}=\varphi_{21}=1/(2+2\nu_s)$, $\gamma_{11}=\gamma_{22}=1$ and $\gamma_{12}=\gamma_{21}=0$, where ν_s is Poisson's ratio. Here δ_{ij} is the Kronecker delta function. Here F_{ext} is the external force exerted by the fluid on the plate, which is determined using the momentum exchange method (Xiong et al. 2020). The initial plate is straight, i.e. $(\partial^2 X^0/\partial s_i^2 \cdot \partial^2 X^0/\partial s_j^2)^{1/2}=0$, where X^0 is the initial position vector. At the two ends of the plate, a simply supported boundary condition is imposed, namely $X=X^0$ and $\partial^2 X/\partial s^2=0$.

To optimize computational efficiency, we exploit symmetry in the problem set-up. For the 2-D cases, a symmetric boundary condition reduces the computational domain to half of the physical domain. In the 3-D cases, a similar strategy is employed, where the computational domain is reduced to a quarter of the full physical domain. This cubic domain is bounded by six planes, with symmetric boundary conditions applied on the two planes that intersect the symmetry axis. At the bottom moving plane, the substrate's wettability is modelled using a Neumann boundary condition (Shao, Shu & Chew 2013), which sets the equilibrium contact angle, θ_e . To improve accuracy, we utilize a weighted least squares method (Pan, Ni & Zhang 2018). It is noted that in our simulations, the contact line is not modelled dynamically: only an equilibrium contact angle is prescribed, with no explicit treatment of contact-line slip. In practice, the apparent contact-line motion in our simulations originates from the implicitly imposed numerical slip length. This simplification is justified by the use of superhydrophobic surfaces, where contact-angle hysteresis is negligible and dynamic contact-line effects have only a minor influence on rebound dynamics (de Goede et al. 2019). Recent studies (Thenarianto et al. 2023) indicate that contact-line effects can become important at smaller Weber numbers, but since our focus is on moderate Weber numbers where inertio-capillary and fluid-structure interaction (FSI) effects dominate, the influence of the numerical slip length remains limited in the present regime. Additional details of the numerical implementation are provided in Xiong et al. (2020). Outflow boundary conditions are applied at the remaining three boundaries.

Here, we provide context for the complexity of the coupled FSI model. The present framework couples a multiphase lattice Boltzmann solver with a finite element solver, transferring fluid stresses to the solid and updating fluid boundaries with the plate displacement. The model also resolves surface wettability and multiphase interfacial dynamics on a moving substrate, which further increases computational complexity compared with conventional single-phase FSI models.

To non-dimensionalize the governing equations, we select ρ_H , D_0 and σ as characteristic quantities. The corresponding reference velocity and time are defined as

Dimensional parameters

Impact velocity, U_0 Droplet diameter, D_0

Liquid/vapour density, ρ_H/ρ_L

Liquid/vapour viscosity, μ_H/μ_L

Surface tension, σ

Plate length, L

Plate thickness, h_s

Plate width (3-D), W

Plate density, ρ_s

Bending stiffness, EI

Stretch stiffness, Eh_s

Reference velocity, $U_{ref} = \sqrt{\sigma/(\rho_H D_0)}$

Reference time, $T_{ref} = \sqrt{\rho_H D_0^3/\sigma}$

Non-dimensional parameters

Weber number, $We = \rho_H U_0^2 D_0 / \sigma$

Bending stiffness, $K_B = EI/(\rho_H U_{ref}^2 L^3)$ Mass ratio, $M_r = \rho_s h_s/(\rho_H L)$

Reynolds number, $Re = \rho_H U_0 D_0 / \mu_H$

Ohnesorge number, $Oh = \sqrt{We}/Re = 0.01$

Stretch stiffness, $K_S = Eh_s/(\rho_H U_{ref}^2 L) = 100$

Density ratio, $\rho_r = \rho_H/\rho_L = 1000$

Viscosity ratio, $\mu_r = \mu_H/\mu_L = 50$

Length ratios, (6 for 2-D and 8 for 3-D)

Width ratio (for 3-D), $W_r = W/D_0 = 3$

Table 1. Summary of dimensional and non-dimensional parameters.

 $U_{ref} = \sqrt{\sigma/(\rho_H D_0)}$ and $T_{ref} = \sqrt{\rho_H D_0^3/\sigma}$, representing the inertia-capillarity time scale. All velocities and times in the following discussion are non-dimensionalized using U_{ref} and T_{ref} , respectively. The key dimensionless parameters governing the problem include the Weber number $We = \rho_H U_0^2 D_0/\sigma$, the bending stiffness $K_B = EI/(\rho_H U_{ref}^2 L^3)$ and the mass ratio $M_r = \rho_s h_s/(\rho_H L)$. Here M_r represents the ratio of plate mass to droplet mass and characterizes the relative inertia of the solid and liquid: small M_r corresponds to a light plate that responds strongly to droplet impact, while large M_r corresponds to a heavier plate with weaker motion. More details of its physical interpretation can be found in Ma & Huang (2025).

We note, however, that M_r is a defined mass ratio, introduced following a convention commonly adopted in FSI studies of elastic plates (Connell & Yue 2007; Hua *et al.* 2014), rather than the true ratio of droplet mass m_d to plate mass m_p . The actual droplet-to-plate mass ratio can be expressed explicitly in terms of M_r and geometric parameters of the system as

$$\frac{m_d}{m_p} = \frac{\rho_H \pi \left(\frac{D_0}{2}\right)^2}{\rho_s h_s L} = \frac{\pi}{4L_r^2 M_r}, \qquad \text{2-D},$$
 (2.4)

$$\frac{m_d}{m_p} = \frac{\rho_H \frac{4}{3}\pi \left(\frac{D_0}{2}\right)^3}{\rho_s h_s L W} = \frac{\pi}{6L_r^2 W_r M_r}, \qquad 3-D,$$
 (2.5)

where $L_r = L/D_0$ and $W_r = W/D_0$ denote the plate length and width ratios, respectively. In our simulations, we use the following values: density ratio $\rho_r = \rho_H/\rho_L = 1000$, dynamic viscosity ratio $\mu_r = \mu_H/\mu_L = 50$, Ohnesorge number $Oh = \sqrt{We}/Re = 0.01$, stretching stiffness $K_S = Eh_S/(\rho_H U_{ref}^2 L) = 100$ and length ratios $L_r = 6$ for 2-D cases, while for 3-D cases, we set $L_r = 8$ and width ratio $W_r = 3$. All dimensional and non-dimensional parameters are summarized in table 1.

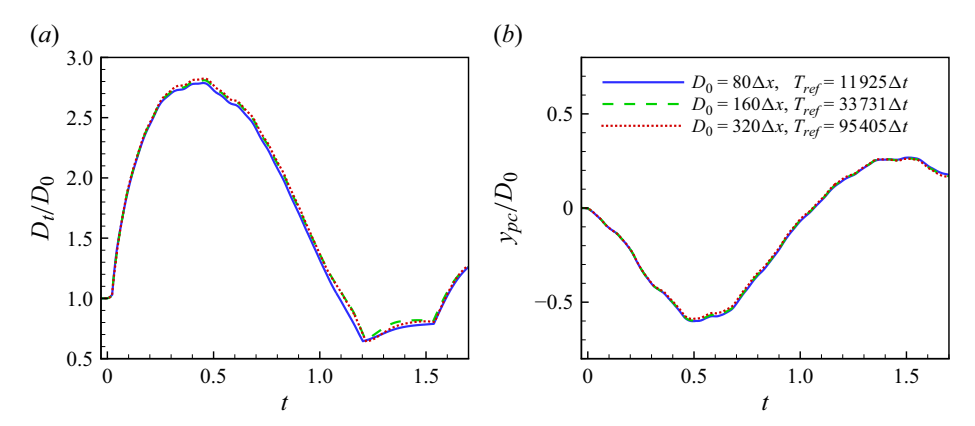


Figure 2. Time evolution of the droplet diameter D_t in (a) and plate centre displacement y_{pc} in (b) for a droplet impacting a flexible plate at We = 30, $K_B = 0.5$ and $M_r = 0.1$, obtained with different grid resolutions and time steps.

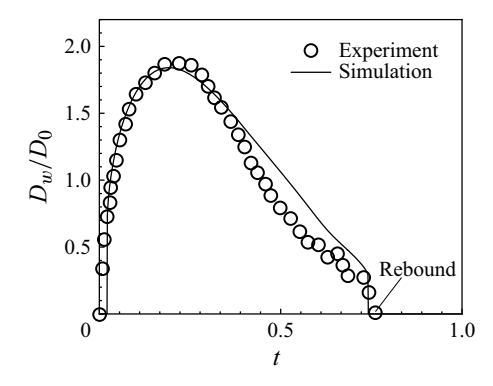


Figure 3. Time evolution of the wetting diameter D_w for a droplet impacting a superhydrophobic rigid surface at We = 55 and Oh = 0.01, comparing experimental and simulation results. The points represent the experimental data from Bird *et al.* (2013), while the line shows the current 3-D simulation results. When D_w returns to zero, it indicates the droplet has bounced off the surface.

A detailed convergence analysis of our numerical framework has been presented in our earlier works (Ma & Huang 2023, 2024). For completeness, and to address the present parameter regime, we have carried out two additional mesh-independence and time step-independence studies: (i) spatial refinement with grid resolutions $D_0 = 80\Delta x$, $160\Delta x$ and $320\Delta x$; (ii) temporal refinement with time steps $T_{ref} = 11925\Delta t$, $33731\Delta t$ and $95405\Delta t$. The time evolutions of the droplet diameter and plate displacement were monitored, and the results (figure 2) show monotonic convergence, with only minor differences between the two finest resolutions. Based on these tests, the resolutions used in the main simulations ($D_0 = 160\Delta x$, $T_{ref} = 33731\Delta t$) are confirmed to lie within the converged regime for all cases studied.

Our numerical methods have been previously validated for simulating droplet interactions with elastic surfaces (Xiong *et al.* 2020; Ma & Huang 2023). Here, we focus on verifying the accuracy of our simulations in capturing droplet rebound dynamics. Figure 3 presents the numerical results for a droplet impacting a rigid superhydrophobic surface, demonstrating strong agreement with experimental data from Bird *et al.* (2013). Additionally, our simulation precisely captures the moment of droplet rebound,

confirming the reliability of our numerical approach in modelling droplet bouncing. In our simulations, the Ohnesorge number is set to Oh = 0.01, slightly larger than the experimental value for water in figure 3. Previous studies (Antonini *et al.* 2013; Maitra *et al.* 2014b; Moqaddam *et al.* 2017) have shown that viscous effects on contact time become significant only for $Oh \gtrsim 0.1$. For Oh < 0.1, viscosity has negligible influence on bounce dynamics, which explains the good agreement between our Oh = 0.01 simulations and the experiments.

3. Results and discussion

Since droplet impact dynamics in two and three dimensions exhibit similar behaviour, as shown in our previous work (Ma & Huang 2023) and validated here, we begin by analysing 2-D cases. These findings are later confirmed by 3-D results in § 3.4. We investigate the effects of three key parameters: the Weber number (We), bending stiffness (K_B) and mass ratio (M_r). All surfaces are superhydrophobic with a contact angle of $\theta_e = 170^\circ$ to ensure rebound.

3.1. Bouncing drops

We conducted simulations across a broad range of parameters: $We \in [10, 60]$, $K_B \in [0.2, \infty)$ and $M_r \in [0.1, 0.4]$, where $K_B = \infty$ represents a rigid plate. The range M_r was chosen to focus on the flexible-plate regime of interest: the lower bound avoids excessively large deformations that would violate the small-displacement assumption (Ma & Huang 2023), and the upper bound excludes cases approaching the rigid-substrate limit. Higher We or lower K_B values are also not considered, consistent with the small-displacement assumption.

Figure 4 illustrates droplet impact dynamics on elastic plates with varying bending stiffness. Upon contact, droplets spread, retract and eventually bounce off due to the superhydrophobic surface, regardless of plate rigidity. In elastic cases, the plate oscillates in response to impact. When it moves upward, it transfers momentum back to the droplet, enabling an earlier rebound – an effect known as the 'springboard effect' (Weisensee *et al.* 2016). Column (v) in figure 4 shows the time evolution of wetting diameter (D_w) and plate centre position (y_{pc}) , characterizing plate motion. Suppose the initial moment is $t_0 = 0$ and D_w returns to zero at time t_b , indicating droplet departure; the contact time (t_c) is defined as the time elapsed since impact: $t_c = t_b - t_0$.

Figure 4 presents five representative cases illustrating three distinct rebound modes – conventional bounce, early bounce and rim rising – corresponding to figure 4(a-e).

The conventional bounce mode appears in cases with low or very high stiffness (figures 4a and 4e, $K_B = 0.2$ and 50, respectively). Here, D_w decreases smoothly to zero during retraction, resembling the rigid case. Contact time is similar to the rigid case, with only slight reductions at lower stiffness.

In the early bounce mode (figures 4b and 4c, $K_B = 0.5$ and 2.0), the droplet lifts off before completing retraction, leading to a discontinuous drop in D_w and a significantly shorter contact time. It is noted that a discrete jump also appears at rebound for the rigid case shown in figure 3. This can be interpreted as follows: near rebound, the droplet's wetted area shrinks rapidly, and surface tension contracts the remaining contact patch abruptly, producing the observed discontinuity. The experimental data in figure 3 show the same behaviour, supporting this interpretation. However, this feature arises from a different mechanism than in the flexible case, where the discontinuity is influenced by the substrate's oscillatory motion and is classified as conventional bounce. It is further observed that this discrete jump does not occur in the rigid reference curve of figure 4.

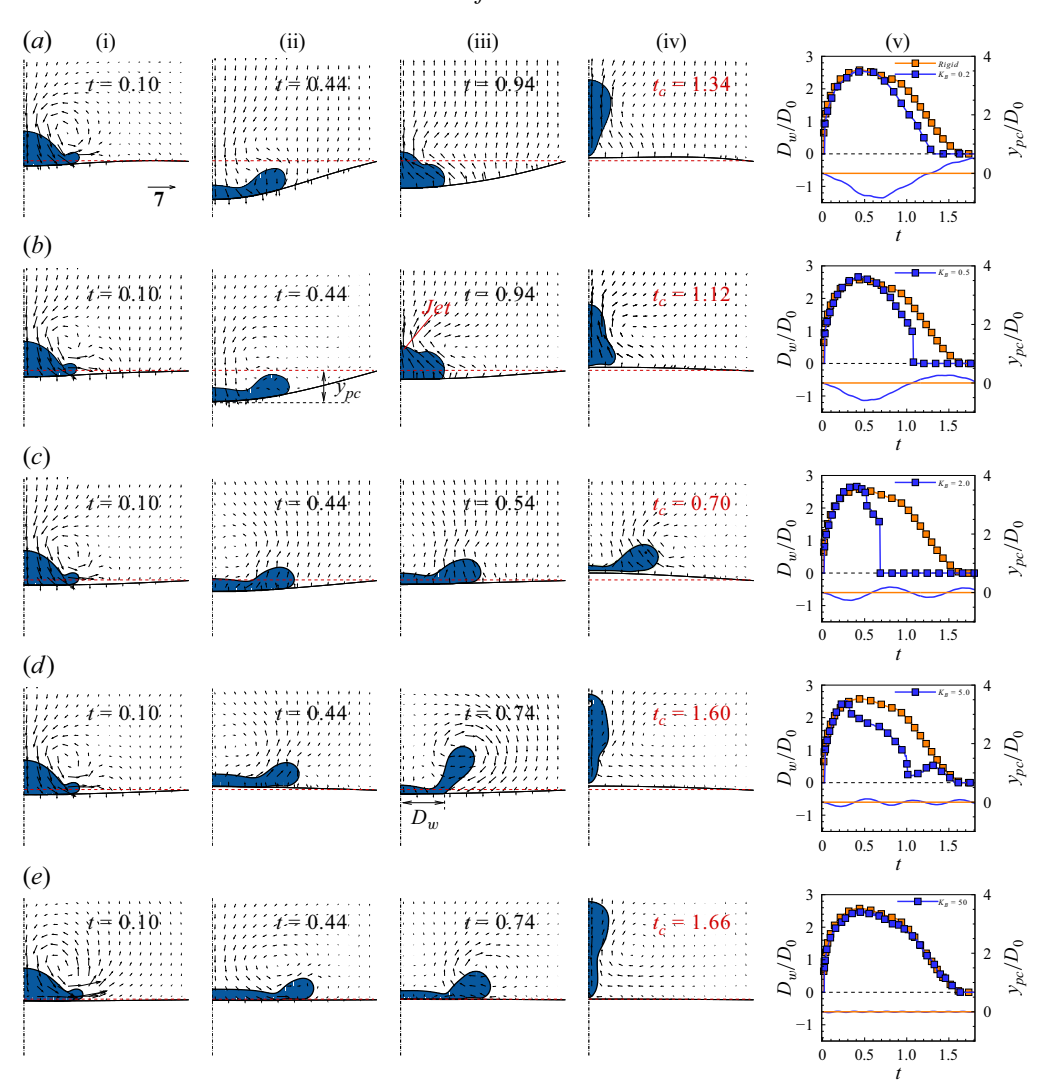


Figure 4. Snapshots of droplet impact on elastic plates at $M_r = 0.1$ and We = 30 for different K_B : (a) $K_B = 0.2$; (b) $K_B = 0.5$; (c) $K_B = 2.0$; (d) $K_B = 5.0$; (e) $K_B = 5.0$. Red dashed lines indicate the plates' initial positions. A uniform reference vector is applied across all cases in (a). Column (v) of snapshots highlights the moments when the droplets detach from the surface. It presents the corresponding time evolution of the wetting diameter D_w (blue line with dots) and the plate centre position y_{pc} (blue line). For comparison, the evolution of D_w and y_{pc} for the rigid case (orange line with dots and orange line, respectively) at the same We are included. The moment D_w returns to zero marks the droplet's departure.

The difference arises from geometry: in 3-D (spherical or axisymmetric) cases, surface-tension effects are stronger, leading to a more pronounced contraction (as in figure 3), whereas in the 2-D (cylindrical) reference of figure 4, surface-tension effects are weaker and the jump is absent.

A central jet forms during retraction due to fluid accumulation. The rebound shape depends on the jet timing: in the postjet bounce (figure 4b), the jet forms before lift-off, producing a columnar rebound. In the prejet bounce (figure 4c), lift-off occurs earlier, yielding a pancake-like shape – previously observed as 'pancake bounce' in experiments

(Vasileiou *et al.* 2016). This scenario results in the greatest reduction in contact time due to minimal retraction.

When the plate becomes stiffer ($K_B = 5.0$, figure 4d), the droplet exhibits the rim-rising mode. Here, only the rim lifts while the centre remains attached. Although D_w decreases quickly, it does not reach zero, indicating incomplete lift-off. During retraction, its value remains consistently smaller than in the rigid case. This mode reduces spreading but does not shorten contact time compared with the rigid case.

Figure 5 shows the distribution of bounce modes in the (We, K_B , M_r) space. The frequency ratio F_r is defined as the ratio between the plate's natural frequency and the characteristic droplet frequency: $F_r = f_{p0}/f_{ref}$, where $f_{ref} = 1/T_{ref} = \sqrt{\sigma/(\rho_H D_0^3)}$, corresponding to the fundamental (n = 2) Rayleigh frequency of a freely vibrating, inviscid droplet (Takaki & Adachi 1985). The Rayleigh frequency can be expressed as

$$f_{Ray} = \frac{\sqrt{2(n-1)n(n+2)}}{\pi} \sqrt{\frac{\sigma}{\rho_H D_0^3}} \quad \text{spherical drop,}$$
 (3.1)

$$f_{Ray} = \frac{\sqrt{2(n-1)n(n+1)}}{\pi} \sqrt{\frac{\sigma}{\rho_H D_0^3}} \quad \text{cylindrical drop.}$$
 (3.2)

The plate frequency f_{p0} is calculated using the fundamental (n = 1) mode of an Euler–Bernoulli beam simply supported at both ends,

$$f_{p0} = \frac{\pi}{2} \sqrt{\frac{EI}{\rho_s h_s L^4}}. (3.3)$$

Rewriting F_r in terms of non-dimensional parameters yields

$$F_r = \frac{\pi D_0}{2L} \sqrt{\frac{K_B}{M_r}}. (3.4)$$

It is noted that the frequency ratio F_r is defined using the prefactor-free scaling $\sqrt{\sigma/(\rho_H D_0^3)}$ of the Rayleigh frequency, which emphasizes relative trends and scaling behaviour. Moreover, because the prefactor differs between 2-D (cylindrical) and 3-D (spherical) geometries, omitting it ensures consistency when comparing results across cases.

From figure 5, it can be seen that at low We (We < 20), early bounce does not occur, consistent with Xiong $et\ al.$ (2020). Here, the impact is too weak to significantly deform the plate and transfer upward momentum to the droplet.

As We increases, early bounce becomes more frequent. The phase diagrams reveal a non-monotonic trend: the system transitions from conventional bounce to early bounce and back to conventional bounce as K_B increases. At low K_B (e.g. figure 4a), the plate oscillates too slowly to transfer momentum in time for early rebound. At moderate K_B (figure 4b,c), the plate responds more quickly, enhancing upward momentum transfer and enabling early bounce. At high K_B (figure 4d), the plate is too stiff to deform significantly. Although it moves upward earlier (higher F_r), the reduced deformation limits momentum transfer, resulting in partial rebound (rim-rising mode). Besides, before the droplet fully detaches, the plate begins to move downward, ceasing to provide additional momentum and thus preventing early bounce. Eventually, at very high K_B (figure 4e), the plate behaves nearly rigidly, and the conventional bounce mode returns.

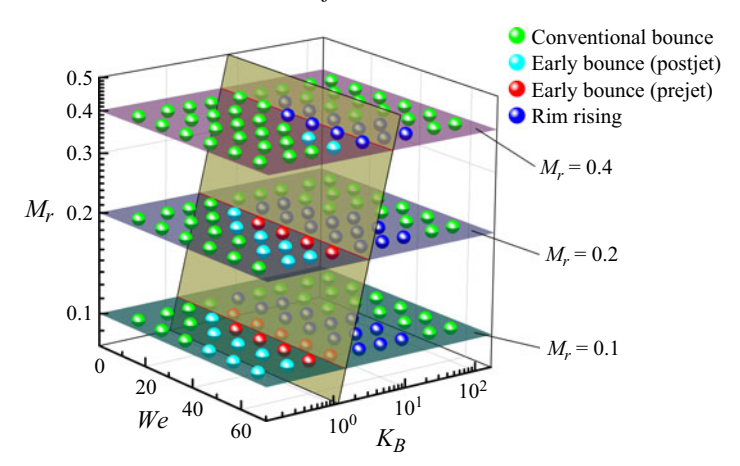


Figure 5. Phase diagrams in the 3-D parameter space (We, K_B , M_r), showing the distribution of bounce modes. Each point corresponds to a simulated case. The inclined plane denotes the boundary where the frequency ratio $F_r \sim 1$, marking the resonance condition between the plate and droplet oscillation frequencies.

The rim-rising mode acts as a transitional regime between early and conventional bounce. As it yields little contact time reduction, it may be considered a variant of conventional bounce.

Figure 5 shows that increasing M_r reduces the prevalence of early bounce and enlarges the conventional bounce region. This is because larger M_r lowers f_{p0} , delaying plate motion and weakening momentum transfer – similar to the effect of low K_B . A 'heavier' plate also moves less overall, further suppressing early bounce.

In summary, early bounce only occurs when f_{p0} is in a moderate range – not too low or too high. Pancake bounce, a subset of early bounce, appears near $F_r \approx 1$, where the droplet and plate frequencies match. This matches the experimental findings of Vasileiou *et al.* (2016). However, for $M_r = 0.4$, pancake bounce is absent even at $F_r \approx 1$, due to the plate's minimal movement.

Figure 6 further clarifies this with the 'bouncing-off phase' φ_b , defined in figure 6(a) as the phase at which the droplet lifts off, relative to the plate's oscillation. The phases at which $y_{pc} = 0$ are assigned values of $\varphi_b = 0$, π , 2π , 3π , etc., in chronological order. Given a bouncing-off moment t_b occurring between two successive zero-crossings at t_1 and t_2 , the corresponding bouncing-off phase φ_b is interpolated linearly between $\varphi_b(t_1)$ and $\varphi_b(t_2)$. For the case illustrated in figure 6(a), φ_b is therefore expressed as

$$\varphi_b(t_b) = [\varphi_b(t_2) - \varphi_b(t_1)] \frac{t_b - t_1}{t_2 - t_1} + \varphi_b(t_1). \tag{3.5}$$

Figure 6(b,c) show that early bounce events (blue symbols) consistently occur in the range $\varphi_b \in (\pi, 3\pi/2)$. For $\varphi_b < \pi$ (e.g. $K_B = 0.2$, $M_r = 0.4$), the plate does not rise until the droplet detached, preventing early lift-off. At $\varphi_b > 3\pi/2$, typical of high K_B , the plate has already reversed motion before droplet detachment, also suppressing early bounce.

Thus, the bouncing-off phase confirms that early bounce requires synchronized plate motion – specifically, upward motion at the right moment – only achievable at moderate oscillation frequency.

3.2. Momentum analysis

To investigate momentum transfer between the droplet and the plate, we focus on the early bounce mode – the only regime that significantly reduces contact time (see figure 5).

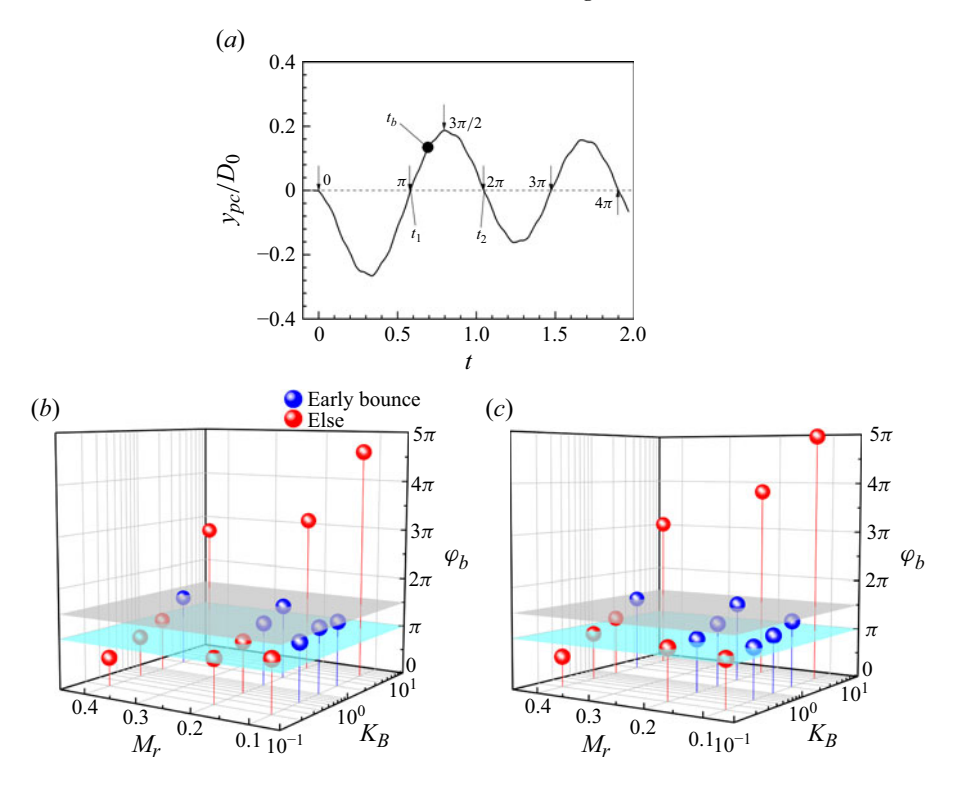


Figure 6. (a) Schematic definition of the bouncing-off phase φ_b , which represents the phase of the plate's oscillation (y_{pc}) at the moment the droplet lifts off (t_b) . The phase is measured relative to successive zero-crossings of y_{pc} . (b) Bouncing-off phase φ_b as a function of K_B and M_r at We = 30. (c) Same as (b), but at We = 60. Blue symbols indicate early bounce cases, while red symbols correspond to other bounce modes. The region between the two shaded planes highlights the phase window $\varphi_b \in (\pi, 3\pi/2)$, where early bounce is most likely to occur.

The analysis is restricted to cases with $K_B \leq 2$. Momentum is normalized by $m_d U_{ref}$, where m_d is the droplet mass. The total vertical momentum is defined as

$$M_{y} = \int_{\Omega} \rho_{H} v d\Omega, \qquad (3.6)$$

where Ω denotes the droplet volume and v the vertical fluid velocity.

Figure 7 shows the contact time t_c versus the vertical momentum at rebound, M_{yc} , for various K_B , We and M_r values in the early bounce regime. Contrary to intuition, t_c increases with M_{yc} and decreases with K_B . One might expect that a droplet with higher upward momentum would lift off sooner, but the data reveal the opposite: more momentum correlates with longer contact times.

To explain this unexpected trend, we examine the time evolution of M_y in figure 8. For droplets on a rigid plate, downward momentum drops sharply upon impact, and energy is quickly redistributed laterally, then partially recovered as upward momentum during retraction. In contrast, on elastic plates, the droplet's downward momentum ($|M_y|$) decreases more gradually due to the plate's own motion. As K_B decreases, the plate's deformation becomes more pronounced, which slows the rate at which the droplet's momentum decreases. Once the plate begins to move upwards, the droplet starts gaining upward momentum.

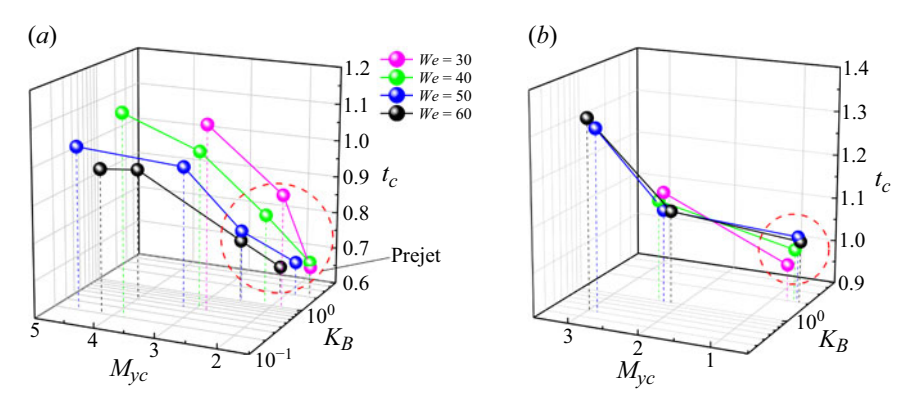


Figure 7. Contact time t_c as a function of vertical momentum at rebound (M_{yc}) and K_B for different Weber numbers: (a) $M_r = 0.1$, (b) $M_r = 0.2$. Only cases exhibiting the early bounce mode, as identified in figure 5, are shown. Symbols inside dotted red circles represent 'prejet bounce' cases; all others correspond to 'postjet bounce' cases.

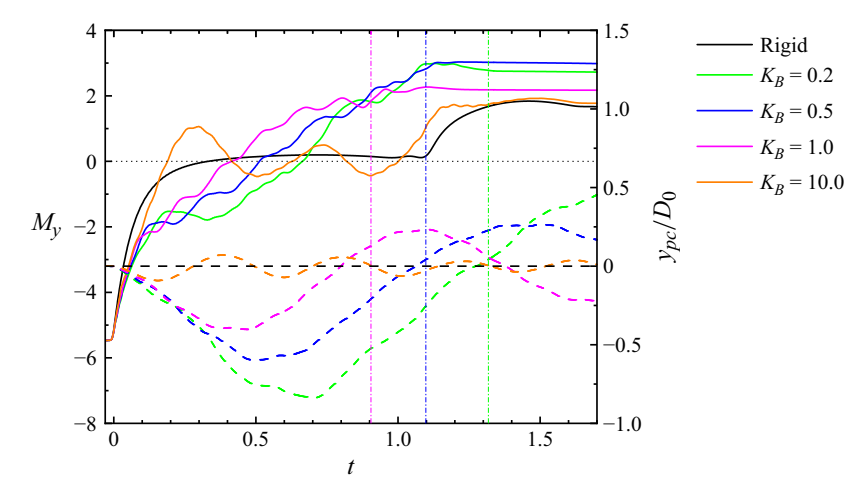
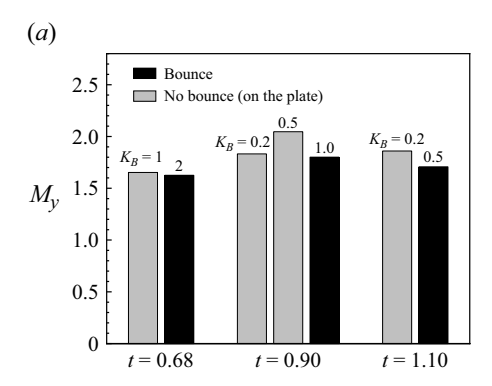


Figure 8. Time evolution of the droplet's total vertical momentum M_y (solid lines) and the vertical position of the plate centre y_{pc} (dashed lines) for various K_B values at $M_r = 0.1$ and We = 30. Coloured dot–dash lines mark the rebound moments for each corresponding K_B case.

For high K_B (e.g. $K_B = 10$), the plate oscillates up and down before the droplet rebounds due to its high vibration frequency (see the orange dashed line). As a result, M_y fluctuates around zero until the droplet eventually lifts off. In contrast, at moderate and lower K_B , M_y increases approximately steadily before lift-off. In these cases, the plate first moves downwards and then upwards, and the droplet rebounds during the upward motion (see the dashed lines), typically within the plate's first vibration cycle. Specifically, the droplet lifts off when the plate reaches approximately $y_{pc} = 0$ (see the dot-dashed lines). At this moment, the plate's upward velocity peaks, and momentum transfer to the droplet ends. Thus, a longer vibration period (i.e. lower frequency, applicable only in early-bounce cases) allows more time for momentum to accumulate, resulting in a larger M_y . In other words, longer contact time leads to greater momentum buildup before rebound, explaining the observed positive correlation between t_c and M_{yc} in figure 7.

Despite the overall correlation, figure 8 shows that droplets with similar vertical momentum can exhibit different rebound behaviours. For instance, at $K_B = 1.0$, the droplet



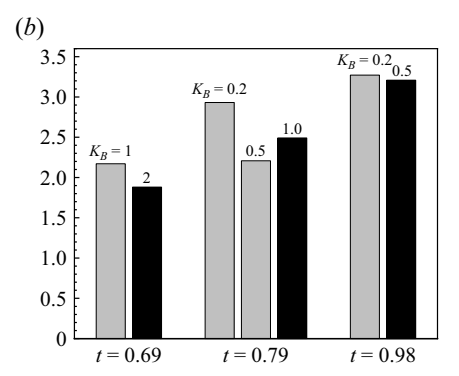


Figure 9. Droplet vertical momentum M_y at selected moments for various K_B values, with $M_r = 0.1$ at (a) We = 30 and (b) We = 50. Each moment corresponds to the rebound moment of one case. Dark bars indicate cases where the droplet has rebounded at that moment; light bars represent cases where rebound has not yet occurred. Cases beyond the rebound moment are not shown.

rebounds at t = 0.9, while droplets at $K_B = 0.5$ and 0.2 – with comparable momentum – do not. A similar discrepancy occurs at t = 1.1: the droplet at $K_B = 0.5$ rebounds, but the one at $K_B = 0.2$, despite having nearly the same momentum, does not.

To verify that this behaviour is not incidental, we present additional cases in figure 9, which shows M_y at key time instants for various K_B values at We = 30 and 50. Dark bars indicate rebound, while light bars represent cases where the droplet remains on the plate. The results confirm that similar total momentum does not ensure rebound. For example, at t = 0.68 in figure 9(a), the droplet rebounds for $K_B = 2.0$ but not for $K_B = 1.0$, despite comparable momentum. The cases from the previous paragraph are also included at t = 0.90 and t = 1.10. Similarly, in figure 9(b), the droplet at $K_B = 0.5$ rebounds at t = 0.98, even though its M_y is nearly equal to or lower than that of the $K_B = 0.2$ case, which does not rebound.

These findings suggest that total momentum alone does not determine rebound behaviour. To understand why, we examine the internal momentum distribution within the droplet. Figure 10(a) shows the vertical velocity fields at t = 0.90, the rebound time for $K_B = 1.0$. At this moment, the elastic cases exhibit broader regions of high vertical velocity (red areas) compared with the rigid case. While all elastic cases gain more upward momentum due to the plate's motion, their internal momentum distributions differ significantly.

For $K_B = 0.2$ and 0.5, a narrow central jet forms, concentrating momentum near the axis. This localized jet absorbs energy but contributes little to lifting the droplet as a whole. In contrast, at $K_B = 1.0$, the jet is just forming, allowing most of the upward momentum to support rebound. This explains why similar total M_y values lead to rebound in one case and not the others (see figure 9a).

Because of this jet effect, lower K_B cases require additional upward force from the plate to achieve rebound – resulting in delayed lift-off and longer contact time. This distinction defines the postjet bounce mode (jet forms before rebound) and the prejet bounce mode (rebound occurs before jet formation). As shown in figure 7, postjet bounces are consistently associated with higher M_{γ} and longer t_c .

The delayed jet formation at higher K_B values arises from the droplet's spreading dynamics. As shown in figure 10(b), a higher K_B ($K_B = 1.0$) results in a greater maximum spreading diameter (see the peaks of the curves). Since the retraction speeds are similar

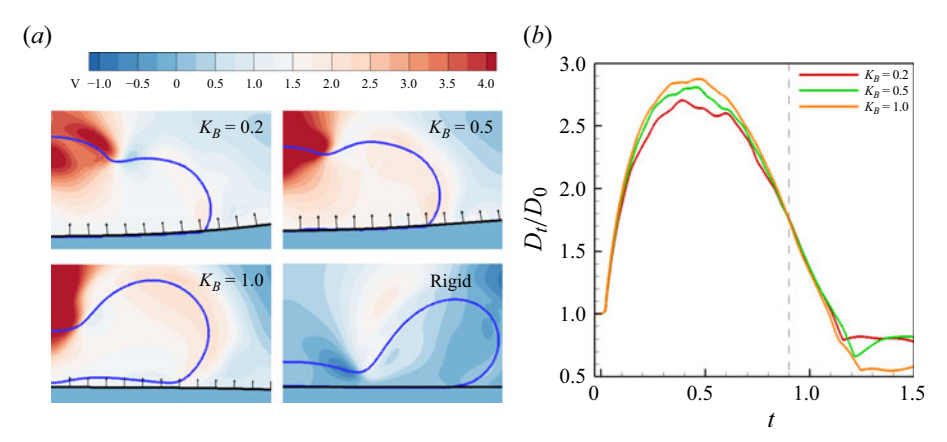


Figure 10. (a) Vertical velocity contours for rigid and elastic cases with various K_B values at We = 30 and $M_r = 0.1$, captured at t = 0.90 – the rebound moment for $K_B = 1.0$. (b) Time evolution of the droplet's spreading diameter D_t for the elastic cases shown in (a). The dashed line marks t = 0.90.

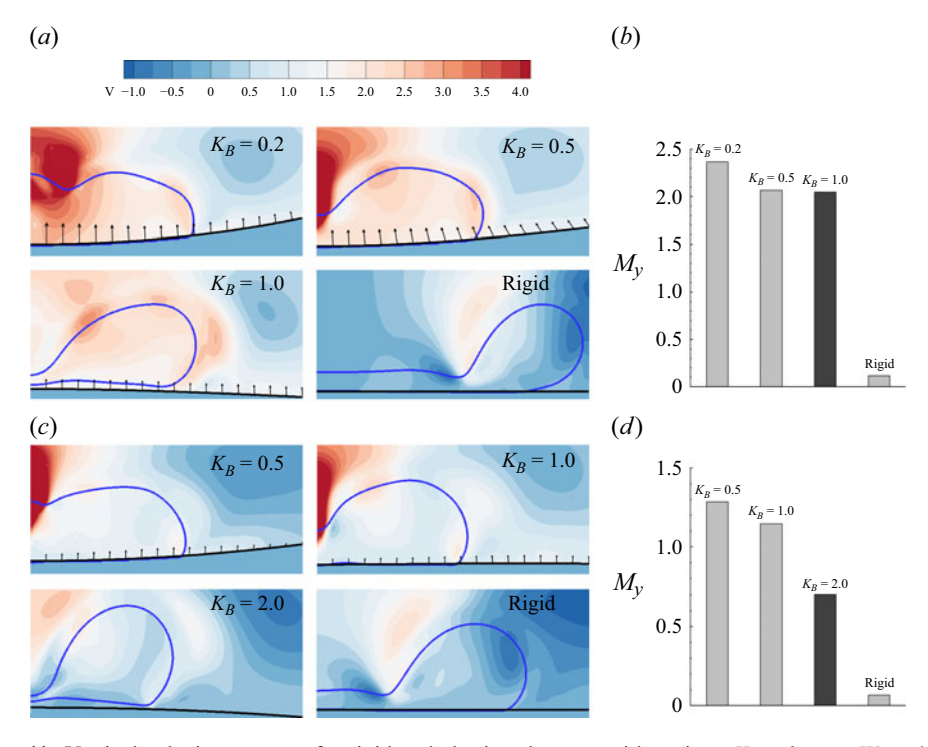


Figure 11. Vertical velocity contours for rigid and elastic substrates with various K_B values at We = 40: (a) $M_r = 0.1$ at t = 0.86, when rebound occurs for $K_B = 1.0$; (c) $M_r = 0.2$ at t = 1.02, when rebound occurs for $K_B = 2.0$. Corresponding total vertical momentum M_y is shown in (b) and (d); dark bars denote cases where the droplet has rebounded.

(as indicated by the slope of the lines during the retraction phase), the fluid takes longer to gather at the centre, delaying jet formation.

This explanation is supported by the cases shown in figure 11. In figure 11(a), at t = 0.86, the droplet rebounds only for $K_B = 1.0$. The corresponding momentum bars in figure 11(b) indicate that total M_V is not a reliable predictor – only the $K_B = 1.0$ case lacks

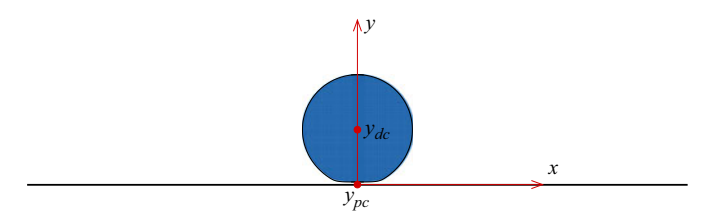


Figure 12. A schematic diagram of the drop-plate system modelled as two interacting spring oscillators. The droplet is supposed to be the upper oscillator. The horizontal plate is supposed to be the lower oscillator, which heaves up and down. Here y_{dc} and y_{pc} denote the centre positions of the droplet and the plate, respectively.

a central jet. Similarly, figure 11(c) shows that rebound occurs only at $K_B = 2.0$ (no jet is present), even though lower K_B cases exhibit greater momentum (figure 11d). Once again, figure 11 demonstrates that the jet diverts momentum otherwise needed for rebound.

These findings reveal that not only the amount of momentum transferred from the plate but also its spatial distribution within the droplet determines whether rebound occurs. A central jet traps upward momentum and delays lift-off, meaning that postjet bounces require more M_y and result in longer contact times. In contrast, prejet bounces – where momentum remains more uniformly distributed – enable earlier rebound with less M_y . Thus, contrary to intuition, more momentum does not always lead to a faster rebound. To promote early detachment, jet formation should be avoided.

3.3. Contact time prediction

This section presents a theoretical model to predict the contact time of a droplet impacting an elastic surface. The droplet–plate interaction is modelled as a coupling between two oscillators (Chantelot *et al.* 2018; Xiong *et al.* 2020), as illustrated in figure 12. Both the droplet and the plate are represented as springs, with their vibrations described by the time evolution of their central positions, y_{dc} and y_{pc} , respectively,

$$y_{dc}(t) = A_d \sin(2\pi f_d t + \pi) + 0.5D_0, \quad y_{pc}(t) = A_p \sin(2\pi f_p t + \pi).$$
 (3.7a-b)

Here, A_d and A_p are the vibration amplitudes, and f_d and f_p are the frequencies of the droplet and plate, respectively. Initially, the droplet rests at a height equal to its radius above the plate (figure 12). Equation (3.7) is introduced as a simplified approximation of the coupled system, retaining the dominant physics while remaining analytically tractable. The neglected higher-order coupling terms are shown to be quantitatively small (see the discussion on f_p), supporting the validity of this assumption. To further justify this ansatz, we include additional numerical comparisons (see figure 13), which demonstrate good agreement between (3.7a) and the fully coupled droplet–substrate dynamics.

It is noted that the model assumes a time-symmetric rebound, which is invalid for rigid cases. As shown in figure 4, droplet rebound on rigid surfaces is highly time-asymmetric. While viscous dissipation contributes to this asymmetry (Villermaux & Bossa 2011), recent studies have demonstrated that inertio-capillary effects alone can also break time symmetry, even for inviscid droplets at intermediate We (Thenarianto $et\ al.\ 2023$; Lin $et\ al.\ 2024$; Gabbard $et\ al.\ 2025$). However, the situation is different on a flexible substrate. For a sufficiently flexible plate (e.g. $K_B = 0.5$ in figure 4b), the retraction phase is significantly shortened. In this early-bounce regime, viscous effects are negligible relative to capillarity, and part of the droplet's inertial energy is transferred to the plate. This energy exchange weakens the inertio-capillary asymmetry, so that the droplet dynamics become approximately time-symmetric prior to lift-off. Beside, we verify this time-symmetry by fitting the droplet centroid trajectory $y_{dc}(t)$ with a sinusoidal function of (3.7a)

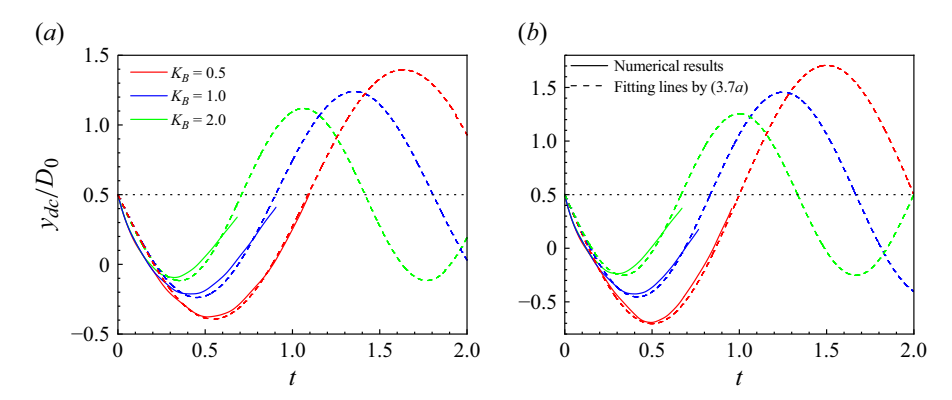


Figure 13. Temporal evolution of the droplet centre displacement y_{dc} for various K_B (solid lines) at $M_r = 0.1$: (a) We = 30, and (b) We = 60. Only the stage prior to rebound is shown. The dashed lines denote sinusoidal fits of the form $y = c_1 \sin(c_2 x + \pi) + 0.5$ (see (3.7a)), where c_1 and c_2 are fitting constants.

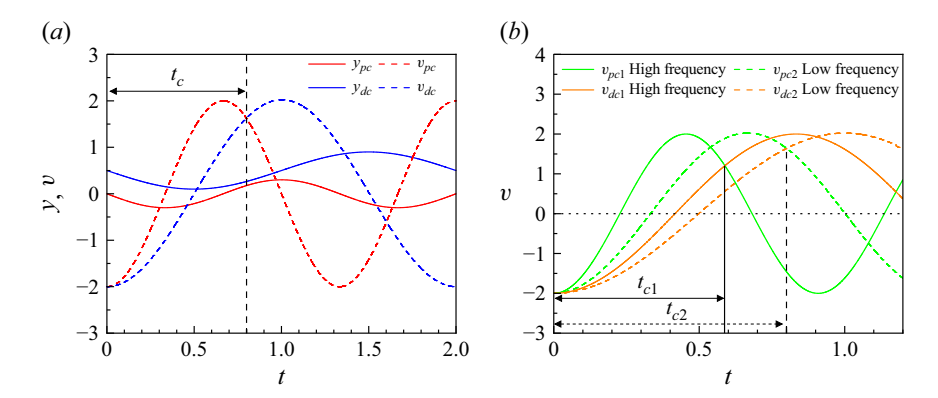


Figure 14. (a) Schematic of time evolution for the central positions and vertical velocities (v_{dc}, v_{pc}) of the droplet and plate. The contact time t_c is the period from t = 0 to the moment when $v_{dc} = v_{pc}$. (b) Schematic of time evolution for the vertical velocities of the droplet (v_{dc1}, v_{dc2}) and the plate (v_{pc1}, v_{pc2}) at high (solid lines) and low (dashed lines) frequencies. The velocity crossover occurs earlier at higher frequency.

(see figure 13). Thus, the model is specifically intended to describe this unique early-bounce regime.

The corresponding vertical velocities, v_{dc} and v_{pc} , are obtained by differentiating (3.7),

$$v_{dc}(t) = 2\pi A_d f_d \cos(2\pi f_d t + \pi), \quad v_{pc}(t) = 2\pi A_p f_p \cos(2\pi f_p t + \pi).$$
 (3.8a-b)

Note that v_{dc} represents the time rate of change of the droplet's centre position in the vertical direction, which differs from the bulk or average velocity of the droplet.

To determine the rebound moment, we compare the time evolution of v_{dc} and v_{pc} , as shown in figure 14(a). Initially, both the droplet and the plate move downward, with the droplet spreading and its centre descending. During this phase, v_{dc} exceeds v_{pc} . After reaching its maximum downward displacement, the plate begins to move upwards, while the droplet may still be in the spreading phase. As retraction begins, the droplet's centre rises. If v_{dc} surpasses v_{pc} during this upward motion, rebound occurs. Therefore, the moment when $v_{dc} = v_{pc}$ defines the rebound moment, as illustrated in figure 14(a).

The numerical simulations discussed above already capture the occurrence of early rebound. The added value of the reduced-order model is that it distils the dynamics into a low-dimensional description, which makes the underlying parameter dependence

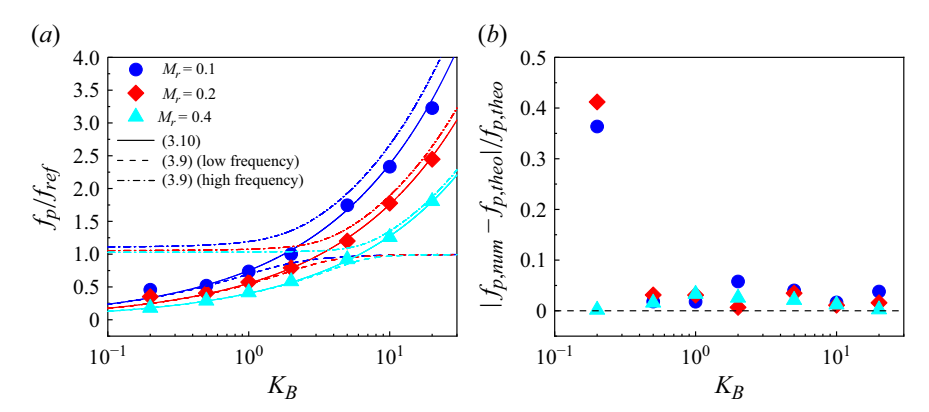


Figure 15. (a) Comparison of plate vibration frequencies from simulations (symbols) and theory (lines) for various K_B and M_r at fixed We = 30. (b) Relative error between numerical results and theoretical prediction (3.10).

transparent. In particular, the model provides a quantitative relation between the plate and droplet oscillation phases, from which it follows directly that the velocity crossover between v_{pc} and v_{dc} must shift monotonically earlier as frequency increases with higher K_B (see figure 14b). This prediction explains, in a concise form, the systematic decrease of contact time t_c with K_B observed in the simulations (figure 7). Thus, while the numerical model reproduces the phenomenon in detail, the reduced model highlights the essential mechanism and offers a quantitative framework for interpreting and generalizing the simulation results.

To evaluate v_{dc} and v_{pc} , the vibration frequencies and amplitudes of both the droplet and plate $(f_d, f_p, A_d \text{ and } A_p)$ must be determined. Two models for f_p exist in the literature. One accounts for the coupled dynamics between droplet and plate (Chantelot *et al.* 2018; Xiong *et al.* 2020), yielding two natural frequencies,

$$f_p/f_{ref} = \sqrt{\frac{1}{2}(1 + F_r^2 + 1/m_r)(1 \pm \sqrt{1 - \epsilon})},$$
 (3.9)

where $m_r = m_p/m_d$, and $\epsilon = 4F_r^2/(1 + F_r^2 + 1/m_r)^2$. Here m_p is the plate mass defined as $m_p = \rho_s V_p$, where V_p is the plate volume. For the 2-D formulation, $V_p = h_s L$ with unit width, while in 3-D cases $V_p = h_s L W$. The ' \pm ' sign corresponds to the high and low frequencies. A detailed derivation is provided by Xiong *et al.* (2020).

An alternative model treats the droplet as a static mass on the plate, neglecting its oscillation (Soto *et al.* 2014; Ma & Huang 2023),

$$f_p = \sqrt{\frac{m_p}{m_p + m_d}} f_{p0}. (3.10)$$

To compare the numerical results and theoretical prediction of f_p , we extract the numerical frequency from the time-domain response of the plate centroid trajectory $y_{pc}(t)$ (figure 6a). Successive peak–trough intervals are measured to calculate the oscillation period, and the frequency f_p is taken as the inverse of the mean period. Only the phase preceding droplet rebound was analysed to ensure consistency. For trajectories with fewer than two full cycles, half- or quarter-cycle durations are used ($f_p = 1/(2\Delta T)$) or $f_p = 1/(4\Delta T)$).

Figure 15(a) shows that the low- and high-frequency solutions from (3.9) match numerical results at low and high K_B , respectively. Meanwhile, (3.10) performs well

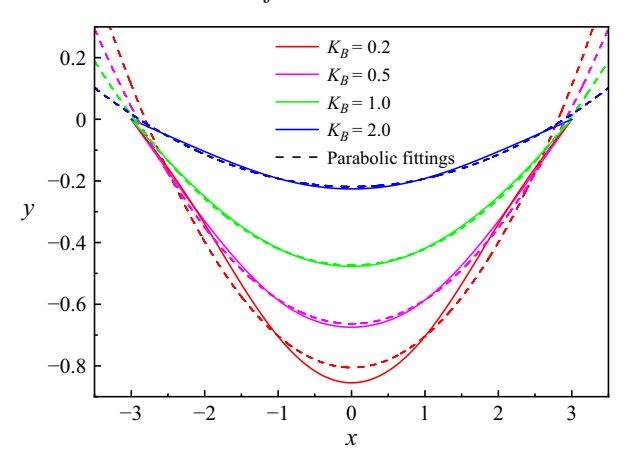


Figure 16. Profiles of the bending plates (solid lines) at a typical moment t = 0.44 after impact for $M_r = 0.1$ and We = 40 with various K_B . The dashed lines show parabolic fits of the form $y = ax^2 + b$, where a and b are fitting constants.

across most K_B values except $K_B = 0.2$, as seen in figure 15(b). This indicates that droplet oscillations exert little influence on plate vibrations, likely due to the small mass ratio $(m_d/m_p \le 0.2)$ and the localized droplet–plate contact. Given the simplicity and accuracy of (3.10), we use it in the following analysis.

Figure 15(b) also shows that the relative error increases for $K_B = 0.2$ with small M_r ($M_r = 0.1$ and 0.2), due to large plate deformation where stretching effects dominate. In these regimes, the small-displacement assumption underlying the Euler–Bernoulli beam theory (used to define f_{p0} , i.e. (3.3)) no longer holds. Thus, cases with low K_B or M_r are excluded from this study.

The plate's vibration amplitude A_p can be estimated from its maximum displacement, d_{max} . According to Ma & Huang (2023), d_{max} can be derived using momentum conservation between the droplet and the plate at the moment of impact. Following Soto *et al.* (2014), we assume a completely inelastic collision at impact, where both centres move together immediately afterward $(U_{dp} = v_{dc}(0) = v_{pc}(0))$, giving

$$A_d f_d = A_p f_p. (3.11)$$

Soto *et al.* (2014) assumed a parabolic deflection of the plate. It is validated here by direct comparison with our simulation data, as shown in figure 16, parabolic fits match the plate deflection profiles closely across all tested cases. Then the plate momentum becomes

$$2\int_0^{L/2} \rho_s W h_s U_{dp} x^2 / L^2 dx = m_p U_{dp} / 3,$$
 (3.12)

where W is the plate width (unity in two dimensions). Applying momentum conservation, $m_d U_0 = m_d U_{dp} + m_p U_{dp}/3$, yields

$$A_p = \frac{1}{2\pi} \frac{m_d}{m_d + m_p/3} \frac{U_0}{f_p}.$$
 (3.13)

This scaling has been validated against simulations in prior work (Ma & Huang 2023).

To determine f_d and A_d , one more equation is needed in addition to (3.11). At the time $t_m = 1/(4f_d)$ – when the droplet's centre reaches its lowest position – A_d can be expressed as the sum of the plate's displacement at t_m and the droplet's radius (see figure 17),

$$A_d = 0.5D_0 - A_p \sin(2\pi f_p/(4f_d) + \pi), \tag{3.14}$$

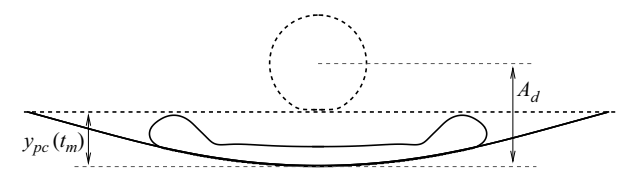


Figure 17. Schematic diagram illustrating how the droplet's vibration amplitude A_d is determined from the maximum displacement of the plate centre y_{pc} . The diagram corresponds to the moment when the droplet's centre reaches its peak position during oscillation.

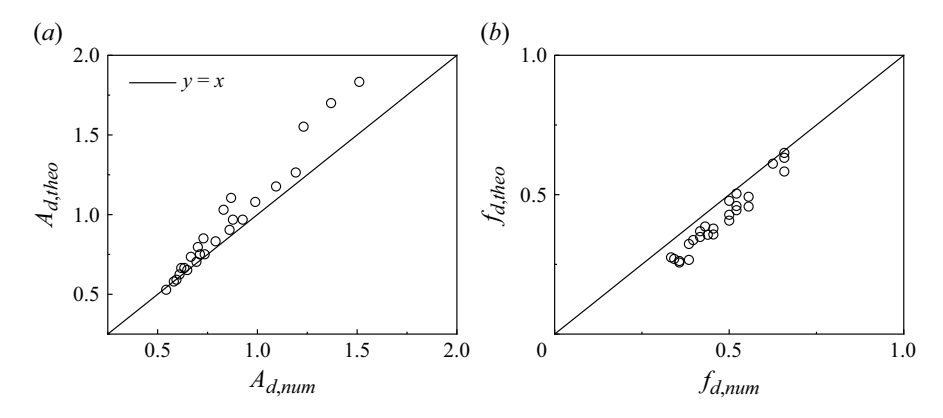


Figure 18. Comparison between numerical results of the droplet oscillation amplitude $A_{d,num}$ (a) and frequency $f_{d,num}$ (b) with the corresponding theoretical predictions ($A_{d,theo}$, $f_{d,theo}$) for various simulated cases exhibiting the early bounce mode. Each point denotes one case.

which neglects half of the thin film thickness at maximum spreading, a small correction.

Equations (3.11) and (3.14) allow implicit solution for f_d and A_d , completing the model. To verify this model, we compare the model predictions for droplet oscillation amplitude and frequency and the corresponding values from full numerical simulations (see figure 18). The droplet frequency is obtained from the fitting lines in figure 13, which show good agreement between the centroid trajectory and sinusoidal profiles. As shown in figure 18, the model systematically overestimates the oscillation amplitude and underestimates the frequency. This discrepancy arises from curvature effects at the dropletsubstrate interface. In the theoretical model, after spreading, the droplet is idealized as a flat 'pancake', with its centre of mass located close to the substrate. In contrast, the numerical simulations reveal a concave meniscus that forms during oscillations (figure 17), lifting the droplet edges above the flat substrate assumed in the model. As a result, for the same plate displacement, the simulated droplet's centre of mass sits higher than predicted, reducing the effective oscillation amplitude. This curvature effect becomes more pronounced at larger amplitudes, explaining the greater deviations observed in figure 18(a). Moreover, the meniscus geometry advances the oscillation phase, causing the droplet to reach its lowest position earlier and thus increasing the apparent frequency. These deviations remain bounded and physically interpretable, confirming that the reduced model still captures the dominant droplet dynamics despite neglecting higher-order effects.

Comparing v_{dc} and v_{pc} using (3.8) yields the contact time t_c (figure 14a). The theoretical predictions are compared with numerical results in figure 19, with detailed values in table 2. For most early-bounce cases, the model agrees well (errors < 15%). Larger deviations for $K_B = 0.2$ are due to the breakdown of beam theory at large deformations.

We	K_B	M_r	$t_{c,num}$	$t_{c,theo}$	Relative error (%)
20	1.0	0.1	0.896	0.847	5.79
20	2.0	0.1	0.695	0.624	10.84
30	0.5	0.1	1.098	1.127	-2.65
30	1.0	0.1	0.905	0.827	9.05
30	2.0	0.1	0.683	0.608	11.60
40	0.2	0.1	1.141	1.688	-38.69
40	0.5	0.1	1.025	1.112	-8.12
40	1.0	0.1	0.845	0.814	3.74
40	2.0	0.1	0.697	0.598	15.30
50	0.2	0.1	1.039	1.673	-46.78
50	0.5	0.1	0.979	1.100	-11.66
50	1.0	0.1	0.793	0.805	-1.45
50	2.0	0.1	0.691	0.590	15.70
60	0.2	0.1	0.988	1.662	-50.86
60	0.5	0.1	0.956	1.091	-13.21
60	1.0	0.1	0.766	0.797	-4.00
60	2.0	0.1	0.672	0.585	13.93
20	2.0	0.2	0.930	0.861	7.74
30	1.0	0.2	1.150	1.137	1.12
30	2.0	0.2	0.983	0.838	15.90
40	1.0	0.2	1.129	1.119	0.89
40	2.0	0.2	1.018	0.824	21.12
50	0.5	0.2	1.314	1.509	-13.82
50	1.0	0.2	1.113	1.106	0.67
50	2.0	0.2	1.038	0.813	24.35
60	0.5	0.2	1.333	1.496	-11.53
60	1.0	0.2	1.106	1.095	1.00
60	2.0	0.2	1.035	0.804	25.11
50	2.0	0.4	1.284	1.153	10.75
60	2.0	0.4	1.315	1.142	14.13

Table 2. Comparison of the contact time between $t_{c,num}$ and $t_{c,theo}$ with detailed parameters. The relative error is defined as $(t_{c,num} - t_{c,theo})/[(t_{c,num} + t_{c,theo})/2]$.

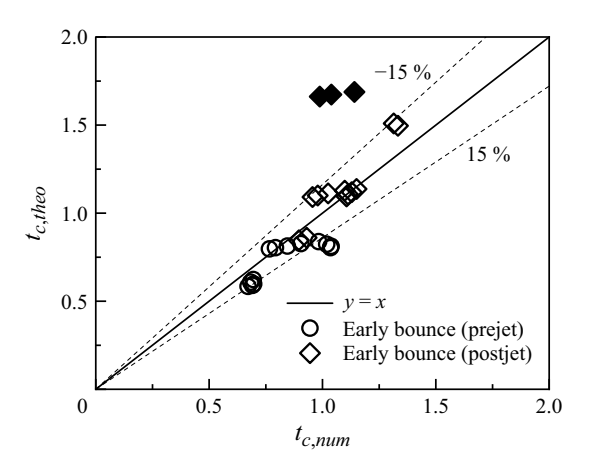


Figure 19. Comparison between numerical results ($t_{c,num}$) and theoretical predictions ($t_{c,theo}$) of the contact time for various simulated cases exhibiting the early bounce mode (see figure 5). Each point represents a case detailed in table 2. Solid symbols indicate cases with $K_B = 0.2$, while the dashed lines mark a ± 15 % error range around the identity line.

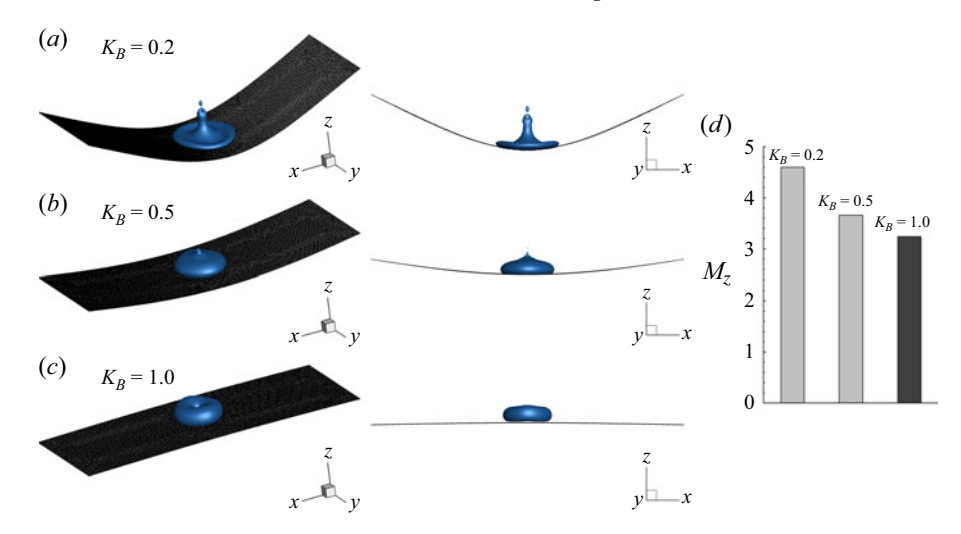


Figure 20. Snapshots of droplets impacting elastic plates in 3-D simulations with different K_B values: (a) $K_B = 0.2$, (b) $K_B = 0.5$ and (c) $K_B = 1.0$, at $M_r = 0.01$ and We = 70. All images are taken at t = 0.43, the moment when the droplet rebounds for $K_B = 1.0$. (d) Total vertical momentum of the droplet, M_z , for the three cases, with the dark bar indicating the rebounding case.

For larger K_B and M_r , the plate behaves more rigidly, and the inelastic collision assumption weakens – leading to larger errors, as seen in the $K_B = 2$, $M_r = 0.2$, We = 60 case (table 2). Despite this, the model remains predictive and is, to our knowledge, the first to estimate droplet contact time on an elastic substrate *a priori*.

Finally, we note that v_{dc} may not fully represent droplet dynamics in cases with strong localized motion (e.g. jet formation during retraction; see figure 4). Thus, the model may be less accurate for 'postjet' early bounces. Nonetheless, figure 19 shows these cases are still well captured, underscoring the model's robustness.

3.4. The 3-D validation

In this section, we validate the novel bounce mechanism described in § 3.2 and the theoretical model proposed in § 3.3 using 3-D simulations. Before doing so, we briefly discuss the computational cost motivating our focus on 2-D simulations. Due to the cubic scaling of the fluid grid and the added complexity of the solid domain, a 3-D case requires orders of magnitude more computational time than its 2-D counterpart. Systematic parameter sweeps are therefore only feasible in 2-D, while 3-D simulations are included for selected cases to validate the mechanisms identified. The simulation set-up is illustrated in figure 1(b). It is noted that the results in § 3.4 are from fully 3-D simulations. The computational domain was reduced to one quarter only by exploiting front—back and left—right symmetry to save computational cost; however, no axisymmetry was imposed in the solver.

Figure 20 presents snapshots of a droplet impacting elastic plates with different K_B values at t = 0.43, which corresponds to the rebound moment for $K_B = 1.0$. At this time, no rebound occurs in the other cases. The corresponding total droplet momentum is shown in figure 20(d). As K_B decreases, the central jet becomes more prominent, consistent with the 2-D results in figure 11. Notably, no jet is observed for $K_B = 1.0$ at this moment. Despite the higher momentum in the softer plates (figure 20d), the droplets do not rebound, corroborating the 2-D findings and supporting the identified bounce mechanism.

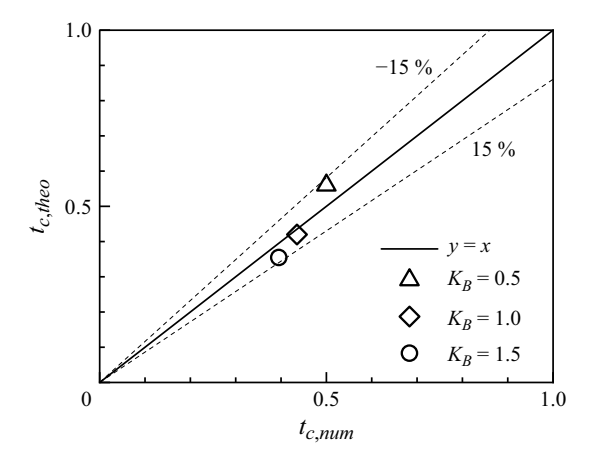


Figure 21. Comparison of contact time between numerical results $(t_{c,num})$ and theoretical predictions $(t_{c,theo})$ for various K_B values at $M_r = 0.01$ and We = 70 in 3-D simulations. The dashed lines mark a $\pm 15\%$ error range around the identity line.

We then assess the theoretical model's ability to predict contact time. Given that variations in We have minimal impact on contact time within our parameter range, a single We value is used for all 3-D cases. Figure 21 compares the theoretical predictions with numerical results, showing good agreement with errors within $\pm 15\%$. This confirms the validity of the proposed model in 3-D scenarios.

4. Conclusion

This study numerically investigates droplet rebound on elastic surfaces and identifies three distinct rebound modes: conventional bounce, early bounce and rim rising. In the early bounce mode, the droplet rebounds before forming a central jet, adopting a pancake shape and exhibiting the shortest contact time, as full retraction is not required. Phase diagrams in the (We, K_B , Mr) space show that early bounce occurs only at moderate oscillation frequency of the plate; plates with very low or very high stiffness fail to induce this mode. Typically, rebound occurs during the bounce-off phase within the range (π , $3\pi/2$). Pancake bounce arises when the natural frequencies of the droplet and plate are comparable, i.e. $F_r \sim 1$.

Momentum analysis reveals that in early bounce, the droplet's vertical momentum (M_{yc}) at rebound increases with contact duration. However, cases with similar or higher total momentum may fail to rebound if that momentum is concentrated in a central jet, which contributes little to lift-off. These cases require additional momentum to achieve rebound, extending the contact time. This insight reveals a new rebound mechanism governed by the spatial distribution of momentum, deepening our understanding of droplet interactions with deformable substrates.

To predict contact time, a theoretical model is proposed by treating the droplet–plate system as two coupled oscillators. The model accurately predicts contact time in early bounce cases, with results aligning closely with simulations and demonstrating robustness across parameter ranges. Finally, 3-D simulations further validate both the identified bounce mechanism and the proposed model.

Funding. This work was supported by the Natural Science Foundation of China (NSFC) grant no.12372253 and by the Supercomputing Center of the USTC.

Declaration of interests. The authors report no conflict of interest.

REFERENCES

- ABOLGHASEMIBIZAKI, M., DILMAGHANI, N., MOHAMMADI, R. & CASTANO, C.E. 2019 Viscous droplet impact on nonwettable textured surfaces. *Langmuir* **35** (33), 10752–10761.
- ANTONINI, C., BERNAGOZZI, I., JUNG, S., POULIKAKOS, D. & MARENGO, M. 2013 Water drops dancing on ice: how sublimation leads to drop rebound. *Phys. Rev. Lett.* 111, 014501.
- BHUSHAN, B., JUNG & Y.C. 2011 Natural and biomimetic artificial surfaces for superhydrophobicity, self-cleaning, low adhesion, and drag reduction. *Prog. Mater. Sci.* 56 (1), 1–108.
- BIANCE, A.-L., CHEVY, F., CLANET, C., LAGUBEAU, G. & QUÉRÉ, D. 2006 On the elasticity of an inertial liquid shock. *J. Fluid Mech.* **554**, 47–66.
- BIRD, J.C., DHIMAN, R., KWON, H.-M. & VARANASI, K.K. 2013 Reducing the contact time of a bouncing drop. *Nature* 503 (7476), 385–388.
- BLOSSEY, R. 2003 Self-cleaning surfacesvirtual realities. Nat. Mater. 2 (5), 301–306.
- CHANTELOT, P., COUX, M., CLANET, C. & QUÉRÉ, D. 2018 Drop trampoline. Europhys. Lett. 124 (2), 24003.
- CHENG, X., SUN, T.-P. & GORDILLO, L. 2022 Drop impact dynamics: impact force and stress distributions. *Annu. Rev. Fluid Mech.* **54** (1), 57–81.
- CLANET, C., BÉGUIN, C., RICHARD, D. & QUÉRÉ, D. 2004 Maximal deformation of an impacting drop. J. Fluid Mech. 517, 199–208.
- CONNELL, B.S.H. & YUE, D.K.P. 2007 Flapping dynamics of a flag in a uniform stream. *J. Fluid Mech.* 581, 3367.
- DERBY, B. 2010 Inkjet printing of functional and structural materials: fluid property requirements, feature stability, and resolution. *Annu. Rev. Mater. Res.* 40, 395–414.
- DHIMAN, R., MCDONALD, AÉ G. & CHANDRA, S. 2007 Predicting splat morphology in a thermal spray process. *Surf. Coatings Technol.* **201** (18), 7789–7801.
- DOYLE, J.F. 2001 Nonlinear Analysis of Thin-Walled Structures: Statics, Dynamics, and Stability. Springer Science & Business Media.
- DRESSAIRE, E., SAURET, A., BOULOGNE, F. & STONE, H.A. 2016 Drop impact on a flexible fiber. *Soft Matter* 12, 200–208.
- FAN, Y., TAN, Y., DOU, Y., HUANG, S. & TIAN, X. 2023 Reducing the contact time of bouncing droplets on superhydrophobic surfaces: foundations, strategies and applications. *Chem. Engng J.* 476, 146485.
- GABBARD, C.T., AGÜERO, E.A., CIMPEANU, R., KUEHR, K., SILVER, E., BAROTTA, J.-W., GALEANO-RIOS, C.A. & HARRIS, D.M. 2025 Drop rebound at low Weber number. *J. Fluid Mech.* 1019, A25.
- GART, S., MATES, J.E., MEGARIDIS, C.M. & JUNG, S. 2015 Droplet impacting a cantilever: a leaf-raindrop system. *Phys. Rev. Appl.* **3** (4), 044019.
- GAUTHIER, A., SYMON, S., CLANET, C. & QUÉRÉ, D. 2015 Water impacting on superhydrophobic macrotextures. *Nat. Commun.* 6 (1), 8001.
- DE GOEDE, T.C., DE BRUIN, K.G., SHAHIDZADEH, N. & BONN, D. 2019 Predicting the maximum spreading of a liquid drop impacting on a solid surface: effect of surface tension and entrapped air layer. *Phys. Rev. Fluids* 4 (5), 053602.
- Hua, R.-N., Zhu, L. & Lu, X.-Y. 2014 Dynamics of fluid flow over a circular flexible plate. *J. Fluid Mech.* **759**, 56–72.
- HUANG, L., SONG, J., WANG, X., ZHAO, C., LIU, Z. & LIU, J. 2018 Soft elastic superhydrophobic cotton: a new material for contact time reduction in droplet bouncing. *Surf. Coatings Technol.* **347**, 420–426.
- JOSSERAND, C. & THORODDSEN, S.T. 2016 Drop impact on a solid surface. *Annu. Rev. Fluid Mech.* 48, 365–391.
- JOUNG, Y.S. & BUIE, C.R. 2015 Aerosol generation by raindrop impact on soil. Nat. Commun. 6 (1), 1–9.
- KIM, J.-H., ROTHSTEIN, J.P. & SHANG, J.K. 2018 Dynamics of a flexible superhydrophobic surface during a drop impact. *Phys. Fluids* 30 (7), 072102.
- KRAJ, A.G. & BIBEAU, E.L. 2010 Phases of icing on wind turbine blades characterized by ice accumulation. *Renew. Energy* **35** (5), 966–972.
- KREDER, M.J., ALVARENGA, J., KIM, P. & AIZENBERG, J. 2016 Design of anti-icing surfaces: smooth, textured or slippery? *Nat. Rev. Materials* 1 (1), 1–15.
- LAAN, N., DE BRUIN, K.G., BARTOLO, D., JOSSERAND, C. & BONN, D. 2014 Maximum diameter of impacting liquid droplets. *Phys. Rev. Appl.* 2 (4), 044018.
- LI, J., HOU, Y., LIU, Y., HAO, C., LI, M., CHAUDHURY, M.K., YAO, S. & WANG, Z. 2016 Directional transport of high-temperature Janus droplets mediated by structural topography. *Nat. Phys.* 12 (6), 606–612.
- Li, X., Ma, X. & Lan, Z. 2010 Dynamic behavior of the water droplet impact on a textured hydrophobic/superhydrophobic surface: the effect of the remaining liquid film arising on the pillars' tops on the contact time. *Langmuir* **26** (7), 4831–4838.

- LIANG, G. & MUDAWAR, I. 2017 Review of drop impact on heated walls. Intl J. Heat Mass Transfer 106, 103–126.
- LIANG, H., XU, J.R., CHEN, J.X., WANG, H.L., CHAI, Z.H. & SHI, B.C. 2018 Phase-field-based lattice Boltzmann modeling of large-density-ratio two-phase flows. *Phys. Rev. E* **97** (3), 033309.
- LIN, S., SHI, D., ZHOU, L., CHEN, L. & LI, Z. 2024 Probing the contact time of droplet impacts: From the Hertz collision to oscillation regimes. *Phys. Rev. E* 110, L053101.
- LIU, Y., ANDREW, M., LI, J., YEOMANS, J.M. & WANG, Z. 2015 Symmetry breaking in drop bouncing on curved surfaces. *Nat. Commun.* 6 (1), 10034.
- LIU, Y., MOEVIUS, L., XU, X., QIAN, T., YEOMANS, J.M. & WANG, Z. 2014 Pancake bouncing on superhydrophobic surfaces. *Nat. Phys.* 10 (7), 515–519.
- LOHSE, D. 2022 Fundamental fluid dynamics challenges in inkjet printing. Annu. Rev. Fluid Mech. 54 (1), 349–382.
- Lv, C., HAO, P., ZHANG, X. & HE, F. 2016 Drop impact upon superhydrophobic surfaces with regular and hierarchical roughness. *Appl. Phys. Lett.* **108** (14), 141602.
- MA, Y. & HUANG, H. 2023 Scaling maximum spreading of droplet impacting on flexible substrates. J. Fluid Mech. 958, A35.
- MA, Y. & HUANG, H. 2024 Clinching 1/2 scaling: deciphering spreading data of droplet impact. Phys. Rev. Fluids 9, 113601.
- MA, Y. & HUANG, H. 2025 Spreading and retraction dynamics of drop impact onto elastic surfaces. *Phys. Rev. Fluids* 10, 053607.
- MAITRA, T., ANTONINI, C., TIWARI, M.K., MULARCZYK, A., IMERI, Z., SCHOCH, P. & POULIKAKOS, D. 2014a Supercooled water drops impacting superhydrophobic textures. *Langmuir* **30** (36), 10855–10861.
- MAITRA, T., ANTONINI, C., TIWARI, M.K., MULARCZYK, A., IMERI, Z., SCHOCH, P. & POULIKAKOS, D. 2014b Supercooled water drops impacting superhydrophobic textures. *Langmuir* **30** (36), 10855–10861.
- MASSINON, M. & LEBEAU, F. 2012 Experimental method for the assessment of agricultural spray retention based on high-speed imaging of drop impact on a synthetic superhydrophobic surface. *Biosyst. Engng* 112 (1), 56–64.
- MISHCHENKO, L., HATTON, B., BAHADUR, V., TAYLOR, J.A., KRUPENKIN, T. & AIZENBERG, J. 2010 Design of ice-free nanostructured surfaces based on repulsion of impacting water droplets. ACS Nano 4 (12), 7699–7707.
- MOHSENI, M. & AMIRFAZLI, A. 2013 A novel electro-thermal anti-icing system for fiber-reinforced polymer composite airfoils. Cold Reg. Sci. Technol. 87, 47–58.
- MOLACEK, J. & BUSH, J.W.M. 2012 A quasi-static model of drop impact. Phys. Fluids 24 (12), 127103.
- MOQADDAM, A.M., CHIKATAMARLA, S.S. & KARLIN, I.V. 2017 Drops bouncing off macro-textured superhydrophobic surfaces. *J. Fluid Mech.* **824**, 866–885.
- NUYTTENS, D., BAETENS, K., DE SCHAMPHELEIRE, M. & SONCK, B. 2007 Effect of nozzle type, size and pressure on spray droplet characteristics. *Biosyst. Engng* 97 (3), 333–345.
- PAN, J.-H., NI, M.-J. & ZHANG, N.-M. 2018 A consistent and conservative immersed boundary method for MHD flows and moving boundary problems. J. Comput. Phys. 373, 425–445.
- QUÉRÉ, D. 2008 Wetting and roughness. Annu. Rev. Mater. Res. 38 (1), 71–99.
- REGULAGADDA, K., BAKSHI, S. & DAS, S.K. 2018 Droplet ski-jumping on an inclined macro-textured superhydrophobic surface. *Appl. Phys. Lett.* **113** (10), 103702.
- RICHARD, D., CLANET, C. & QUÉRÉ, D. 2002 Contact time of a bouncing drop. *Nature* 417 (6891), 811–811. RICHARD, D. & QUÉRÉ, D. 2000 Bouncing water drops. *Europhys. Lett.* 50 (6), 769.
- SANJAY, V., CHANTELOT, P. & LOHSE, D. 2023 When does an impacting drop stop bouncing? *J. Fluid Mech.* **958**, A26.
- Shao, J.Y., Shu, C. & Chew, Y.T. 2013 Development of an immersed boundary-phase field-lattice Boltzmann method for Neumann boundary condition to study contact line dynamics. *J. Comput. Phys.* **234**, 8–32.
- SHIRI, S. & BIRD, J.C. 2017 Heat exchange between a bouncing drop and a superhydrophobic substrate. *Proc. Natl Acad. Sci.* 114 (27), 6930–6935.
- SOTO, D., DE LARIVIÈRE, AÉLIE B., BOUTILLON, X., CLANET, C. & QUÉRÉ, D. 2014 The force of impacting rain. *Soft Matter* **10** (27), 4929–4934.
- SOUSA, S.C.L., MENDES, A.D.O., FIADEIRO, P.T. & RAMOS, A.M.M. 2014 Dynamic interactions of pigment-based inks on chemically modified papers and their influence on inkjet print quality. *Indust. Engng Chem. Res.* 53 (12), 4660–4668.
- SUN, Q., et al. 2019 Surface charge printing for programmed droplet transport. Nat. Mater. 18 (9), 936-941.
- TAKAKI, R. & ADACHI, K. 1985 Vibration of a flattened drop. ii. normal mode analysis. *J. Phys. Soc. Japan* 54 (7), 2462–2469.

- THENARIANTO, C., KOH, X.Q., LIN, M., JOKINEN, V. & DANIEL, D. 2023 Energy loss for droplets bouncing off superhydrophobic surfaces. *Langmuir* **39** (8), 3162–3167.
- UPADHYAY, G., KUMAR, V. & BHARDWAJ, R. 2021 Bouncing droplets on an elastic, superhydrophobic cantilever beam. Phys. Fluids 33 (4), 042104.
- VASILEIOU, T., GERBER, J., PRAUTZSCH, J., SCHUTZIUS, T.M. & POULIKAKOS, D. 2016 Superhydrophobicity enhancement through substrate flexibility. Proc. Natl Acad. Sci. USA 113 (47), 13307–13312.
- VILLERMAUX, E. & BOSSA, B. 2011 Drop fragmentation on impact. J. Fluid Mech. 668, 412-435.
- VOIGT, C.C., SCHNEEBERGER, K., VOIGT-HEUCKE, S.L. & LEWANZIK, D. 2011 Rain increases the energy cost of bat flight. *Biol. Lett.-UK* 7 (5), 793–795.
- WANG, L., WANG, R., WANG, J. & WONG, T.-S. 2020 Compact nanoscale textures reduce contact time of bouncing droplets. *Sci. Adv.* 6 (29), eabb2307.
- WEI, X., JIA, Z., SUN, Z., FARZANEH, M. & GUAN, Z. 2016 Effect of the parameters of the semiconductive coating on the anti-icing performance of the insulators. *IEEE Trans. Power Delivery* **31** (4), 1413–1421.
- WEISENSEE, P.B., TIAN, J., MILJKOVIC, N. & KING, W.P. 2016 Water droplet impact on elastic superhydrophobic surfaces. *Sci. Rep.* 6 (1), 1–9.
- WISDOM, K.M., WATSON, J.A., Qu, X., LIU, F., WATSON, G.S. & CHEN, C.-H. 2013 Self-cleaning of superhydrophobic surfaces by self-propelled jumping condensate. *Proc. Natl Acad. Sci.* 110 (20), 7992– 7997.
- XIONG, Y.F., HUANG, H.B. & LU, X.Y. 2020 Numerical study of droplet impact on a flexible substrate. *Phys. Rev. E* **101** (5), 053107.
- YARIN, A.L. 2006 Drop impact dynamics: splashing, spreading, receding, bouncing. Annu. Rev. Fluid Mech. 38 (1), 159–192.
- YE, Q. & DOMNICK, J. 2017 Analysis of droplet impingement of different atomizers used in spray coating processes. J. Coat. Technol. Res. 14 (2), 467–476.
- ZHAN, H., LU, C., LIU, C., WANG, Z., LV, C. & LIU, Y. 2021 Horizontal motion of a superhydrophobic substrate affects the drop bouncing dynamics. *Phys. Rev. Lett.* **126** (23), 234503.
- ZHANG, Z., CHI, Y., SHANG, L., ZHANG, P. & ZHAO, Z. 2016 On the role of droplet bouncing in modeling impinging sprays under elevated pressures. *Intl J. Heat Mass Transfer* **102**, 657–668.